MNRAS **429,** 2960–2973 (2013) doi:10.1093/mnras/sts537

CO bandhead emission of massive young stellar objects: determining disc properties★

J. D. Ilee,[1†] H. E. Wheelwright,[2] R. D. Oudmaijer,[1] W. J. de Wit,[3] L. T. Maud,[1] M. G. Hoare,[1] S. L. Lumsden,[1] T. J. T. Moore,[4] J. S. Urquhart[2] and J. C. Mottram[5]

[1]*School of Physics and Astronomy, EC Stoner Building, University of Leeds, Leeds LS2 9JT*
[2]*Max-Planck-Institut für Radioastronomie, Auf dem Hügel 69, D-53121 Bonn, Germany*
[3]*European Southern Observatory, Alonso de Cordova 3107, Vitacura, Santiago, Chile*
[4]*Astrophysics Research Institute, Liverpool John Moores University, Twelve Quays House, Egerton Wharf, Birkenhead CH41 1LD*
[5]*Leiden Observatory, Leiden University, PO Box 9513, NL-2300 RA Leiden, the Netherlands*

Accepted 2012 December 3. Received 2012 November 21; in original form 2012 October 29

ABSTRACT

Massive stars play an important role in many areas of astrophysics, but numerous details regarding their formation remain unclear. In this paper we present and analyse high-resolution ($R \sim 30\,000$) near-infrared 2.3 μm spectra of 20 massive young stellar objects (MYSOs) from the Red *MSX* Source (RMS) data base, in the largest such study of CO first overtone bandhead emission to date. We fit the emission under the assumption it originates from a circumstellar disc in Keplerian rotation. We explore three approaches to modelling the physical conditions within the disc – a disc heated mainly via irradiation from the central star, a disc heated mainly via viscosity, and a disc in which the temperature and density are described analytically. We find that the models described by heating mechanisms are inappropriate because they do not provide good fits to the CO emission spectra. We therefore restrict our analysis to the analytic model, and obtain good fits to all objects that possess sufficiently strong CO emission, suggesting circumstellar discs are the source of this emission. On average, the temperature and density structure of the discs correspond to geometrically thin discs, spread across a wide range of inclinations. Essentially all the discs are located within the dust sublimation radius, providing strong evidence that the CO emission originates close to the central protostar, on astronomical unit scales. In addition, we show that the objects in our sample appear no different to the general population of MYSOs in the RMS data base, based on their near- and mid-infrared colours. The combination of observations of a large sample of MYSOs with CO bandhead emission and our detailed modelling provide compelling evidence of the presence of small-scale gaseous discs around such objects, supporting the scenario in which massive stars form via disc accretion.

Key words: accretion, accretion discs – circumstellar matter – stars: early-type – stars: formation – stars: pre-main-sequence.

1 INTRODUCTION

Massive stars are important from stellar to galactic scales. Their high temperature and luminosity result in the injection of large amounts of ionizing radiation and kinetic energy into their surroundings, which shapes the local interstellar medium (ISM) and may trigger nearby star formation. They also deposit chemically enriched material into the ISM via continuous mass loss during their lifetime and in supernova explosions. However, the formation mechanisms of massive stars ($M \gtrsim 8\,M_{\odot}$) are poorly understood (see the review of Zinnecker & Yorke 2007). Given their importance in stellar and galactic evolution, it is crucial to understand how they form.

The precursors of massive stars, massive young stellar objects (MYSOs), possess a short Kelvin–Helmholtz contraction time-scale (10^{4-5} yr; Mottram et al. 2011a) and thus reach the main sequence and obtain a high luminosity while still enshrouded in their natal cloud material. This high luminosity presents a challenge to theories of massive star formation, particularly when considering a scaled

★Based on observations made with the European Southern Observatory (ESO) Very Large Telescope at the Cerro Paranal Observatory under programme ID 079.C-0725.

†E-mail: pyjdi@leeds.ac.uk

up version of low-mass star formation (as in Shu, Adams & Lizano 1987; see Norberg & Maeder 2000). There is only a short time for the star to accumulate sufficient mass before the protostar ionizes the surrounding material, which, along with significant radiation pressure from the protostar, may halt further accretion (Larson & Starrfield 1971; Kahn 1974; Wolfire & Cassinelli 1987). However, recent 3D hydrodynamic models indicate that discs circumvent the proposed barrier to massive star formation by facilitating the accretion of matter on to the central object (Krumholz et al. 2009; Kuiper et al. 2010, 2011). In addition, observations have shown that some ultra-compact H II regions have outflows, usually associated with ongoing accretion (e.g. Klaassen et al. 2011). Thus, continued accretion must be possible after the star reaches the main sequence and begins ionizing its surroundings.

Confirming the presence of discs around MYSOs presents a considerable observational challenge. Such objects are relatively rare, and still embedded in molecular cloud material, making them optically invisible. There have been a handful of detections of discs around MYSOs (see Patel et al. 2005; Jiménez-Serra et al. 2007; Kraus et al. 2010; Carrasco-González et al. 2012) but the disc properties are difficult to determine. Observations at longer wavelengths (such as the far-infrared and submillimetre) only probe disc properties at large distances from the central protostar. Furthermore, very few studies can be conducted with sufficient angular resolution to probe astronomical unit sized scales, which is necessary to study the inner regions of circumstellar discs. The exception is the observation of the MYSO G310.0135+00.3892 with the Very Large Telescope Interferometer (VLTI) and AMBER (Petrov et al. 2007) reported by Kraus et al. (2010), which achieved a maximum resolution of approximately 10 au. This provided unique information on the geometry of the *K*-band continuum emitting material. However, this study involved only a single object. Therefore, observations of a large sample of MYSOs using an alternative method that can probe close to the central protostar are required.

The inner regions of gaseous discs are difficult to access observationally, especially as near-infrared (NIR) interferometric studies are limited to isolated objects which are bright in the NIR (Tatulli et al. 2008; Wheelwright et al. 2012b). Therefore, to study the inner discs of MYSOs, we must employ indirect methods. The CO molecule is an ideal tracer of these regions because the coupled rotational and vibrational excitation causes a distinctive emission feature, the CO bandhead, so called because they appear in bands in low-resolution spectra. The first overtone $v = 2$–0 bandhead emission at 2.3 μm occurs in warm ($T = 2500$–5000 K) and dense ($n > 10^{11}$ cm^{-3}) gas. These are the conditions expected in the inner regions of accretion discs. This makes CO bandhead emission a valuable tool that allows us to trace these regions. In addition, because this feature is the result of transitions across a range of energy levels (and therefore temperatures), it also allows us to probe the physical properties throughout the disc. Previous studies of CO bandhead emission have been successful in fitting spectra of young stars with a range of masses under the assumption that the emission originates from a circumstellar disc (Carr 1989; Chandler, Carlstrom & Scoville 1995; Bik & Thi 2004; Blum et al. 2004; Davies et al. 2010; Wheelwright et al. 2010), but a study involving a significant number of MYSOs has yet to be performed.

This has been partly due to a lack of a representative sample of MYSOs. Early searches for MYSOs were conducted using the *IRAS* point source catalogue (Molinari et al. 1996; Sridharan et al. 2002). This suffered from source confusion due to the large beam size (2–5 arcmin at 100 μm) and was biased to isolated objects away from the Galactic plane. This issue has been addressed by the Red *MSX* Source (RMS) survey (Lumsden et al. 2002), which is an unbiased survey of MYSOs throughout the Galaxy. It is drawn from the *MSX* mid-infrared survey of the Galactic plane (Egan, Price & Kraemer 2003), which has a resolution of 18 arcsec, allowing detection of sources in previously unresolved regions. An extensive multi-wavelength campaign has been conducted to identify contaminant objects such as ultra-compact H II regions and planetary nebula (Urquhart et al. 2007a, 2009a; Mottram et al. 2007, 2010), finally yielding approximately 500 candidate MYSOs in the data base. Kinematic distance estimates to the MYSOs were obtained from molecular line observations (Urquhart et al. 2007b, 2008; Urquhart, Morgan & Thompson 2009b; Urquhart et al. 2011, 2012), while bolometric luminosities have been determined from fits to the MYSOs' spectral energy distributions (SEDs; Mottram et al. 2011b).

In this paper we study a subset of the RMS data base.[1] We utilize our extensive low-resolution spectroscopic survey of RMS sources (see e.g. Cooper, submitted; Clarke 2007) to select objects for a high-resolution spectroscopic study of CO bandhead emission in MYSOs. We detect CO emission in 20 MYSOs (and two non-MYSOs), which is compared to kinematic models to assess whether the emission originates in circumstellar discs. Finally, we attempt to determine the properties of the CO emitting gas and constrain the accretion rates of these objects. Section 2 outlines the observations we have performed while Section 3 details our modelling. Section 4 presents our observations and model fits to the spectra, along with an analysis of the best-fitting parameters. Section 5 discusses our findings and Section 6 presents our conclusions from this work.

2 OBSERVATIONS AND SAMPLE SELECTION

Table 1 presents the observational parameters of the 20 MYSO, and two non-MYSO targets in our study that possessed CO emission. The data were taken using the CRIRES near-infrared cryogenic spectrograph (Kaeufl et al. 2004) on the Very Large Telescope (VLT) over three nights in 2007 June. A spectral resolution of $R \sim 30\,000$ was achieved ($\Delta\lambda = 0.08$ nm at $\lambda = 2.3$ μm) using a slitwidth of 0.6 arcsec. Standard ABBA nodding along the slit was used. The seeing conditions varied from 0.8 to 1.2 arcsec. single pixel element represents 0.011 nm, while a resolution element covers approximately seven pixels. Using a central wavelength of $\lambda_c = 2.286$ μm, the CO emission spans chips three and four of the detector. The CO bandhead peak is located on the third detector chip. Telluric standard stars of spectral type A, featureless in the wavelength range of interest, were observed between science targets using an identical instrumental set-up and at similar airmasses to ensure similar sky conditions.

The data were reduced using the ESO-provided CRIRES pipeline, via the GASGANO data organiser (version 2.2.7). Dark current was removed and detector linearity corrections applied, and then master flat frames and bad pixel maps were used to correct the spectra. The final spectra were extracted using the optimal extraction algorithm. Wavelength calibration was performed using a cross-correlation with the HITRAN model catalogue (Rothman et al. 1998) and OH lines. The standard stars were reduced and extracted in the same manner. The final spectra were obtained by division of the object spectra by their corresponding standard star to remove telluric spectral features. To further remove the effect of bad pixels, the spectra were cleaned using a sigma-clipping algorithm that removed any

[1] http://www.ast.leeds.ac.uk/RMS/

Table 1. Observed quantities for each object. The bolometric luminosity $L_{\rm Bol}$, 2MASS K-band magnitude and distance $d_{\rm kin}$ are all taken from the RMS database unless otherwise stated.

Object	Associated *IRAS* source	RA (J2000)	Dec. (J2000)	$L_{\rm Bol}$ ($L_\odot$)	K (mags)	$d$kin (kpc)	$t_{\rm int}$ (h)	Blue Shoulder	Chip Four	S/N	CO σ
MYSOs											
G012.9090−00.2607	IRAS18117−1753	18:14:39.56	−17:52:02.3	5.4×10^4	9.2	3.8	5.0	Y	Y	63	12
G033.3891+00.1989	IRAS 18490+0026	18:51:33.82	+00:29:51.0	1.0×10^4	7.2	5.1	0.3	N	Y	81	10
G035.1979−00.7427	IRAS09088−4929	18:58:12.99	+01:40:31.2	3.1×10^4	12.6	2.2	1.6	N	N	18	7
G270.8247−01.1112	IRAS09088−4929	09:10:30.89	−49:41:29.8	9.9×10^3	10.1	7.7	8.3	Y	Y	61	11
G282.2988−00.7769	IRAS 10082−5647	10:10:00.32	−57:02:07.3	8.9×10^3	7.0	5.5	0.1	Y	Y	114	11
G287.3716+00.6444	IRAS 10460−5811	10:48:0455	−58:27:01.5	2.8×10^4	7.5	5.6	0.3	N	N	128	12
G293.8947−00.7825	–	11:32:32.82	−62:15:43.1	1.2×10^4	8.8	10	2.1	N	Y	102	6
G296.2654−00.3901	IRAS 11507−6213	11:53:10.93	−62:30:20.0	4.5×10^3	8.9	8.9	2.1	N	Y	58	8
G305.2017+00.2072	IRAS 13079−6218	13:11:10.45	−62:34:38.6	4.9×10^4	9.4	3.6	2.1	N	Y	63	18
G308.9176+00.1231	IRAS 13395−6153	13:43:01.70	−62:08:51.2	1.4×10^5	6.4	4.6	0.1	Y	N	64	7
G310.0135+00.3892	IRAS 13481−6124	13:51:37.85	−61:39:07.5	5.7×10^4	4.9	3.3	0.1	Y	N	120	8
G332.0939−00.4206	IRAS 16124−5110	16:16:16.46	−51:18:25.2	1.8×10^5	5.9	3.5	0.1	–	N	58	5
G332.9868−00.4871	IRAS 16167−5036	16:20:37.81	−50:43:49.6	2.6×10^4	9.3	3.5	3.3	Y	N	47	10
G338.9377−00.4890	–	16:45:08.23	−46:22:18.5	2.1×10^3	9.1	3.2	2.1	Y	N	50	7
G339.6816−01.2058	IRAS 16474−4610	16:51:05.95	−46:15:52.4	1.6×10^4	8.5	2.6	0.3	–	N	74	4
G347.0775−00.3927	IRAS 17089−3951	17:12:25.81	−39:55:19.9	1.8×10^3	8.5	1.6	2.1	Y	Y	62	7
IRAS08576−4334§	–	08:59:27.40	−43:45:03.7	–	9.4	2.2‖	5.0	N	Y	41	40
IRAS16164−5046§	–	16:20:11.06	−50:53:16.2	1.0×10^5†	9.5†	3.6†	5.0	Y	Y	61	14
IRAS17441−2910§	–	17:44:09.60	−29:10:58.0	5.2×10^5*	5.3	9.8*	0.4	Y	Y	**33**	9
M8E-IR§	IRAS 18018−2426	18:04:53.26	−24:26:42.3	–	4.4	1.9‡	0.2	N	Y	125	12
Non-MYSOs (see Appendix B)											
G332.9457+02.3855	IRAS 16045−4832	16:08:12.08	−48:40:38.5	860	9.7	1.9	0.04	N	Y	36	8
G338.5459+02.1175	IRAS 16289−4449	16:32:32.19	−44:55:30.6	16	7.2	0.3	5.0	N	Y	60	17

§: Object is not a member of the RMS database, but was selected based on previously observed CO emission.
†: From Bik et al. (2006).
‡: From Chini & Neckel (1981).
*: From Walsh et al. (1997).
‖: Kinematic distance from the rotation curve of Brand & Blitz (1993) and $v_{\rm LSR} = 7.5 {\rm kms}\sim^1$(Bronfman et al. 1996).

pixels with a value above three times the standard deviation of the pre-bandhead portion of the spectrum. This was determined to be the maximum amount of cleaning that could be performed without affecting the appearance of real spectral features.

2.1 Observational results

The spectra, presented in Section 4, exhibit a range of bandhead shapes and strengths. 10 objects possess a so-called 'blue shoulder', in which there is prominent emission on the shorter wavelength side of the bandhead peak. This is caused by Doppler-shifted rotational lines, and may be indicative of rotational motion in a circumstellar disc, or an outflowing wind (Kraus et al. 2000). The other 10 objects show steep rises in the bandhead slope. Several objects (e.g. G270.8247−01.1112) possess a residual telluric feature in the pre-bandhead portion of the spectrum, but this did not affect our analysis.

The signal-to-noise ratio of the spectra ranges from approximately 20 to 150. The average bolometric luminosity of the objects is 5×10^4 $L_\odot$, typical of other objects within the RMS survey (Mottram et al. 2011a). The objects are generally bright in the K band, but this is a selection effect based on observational requirements.

The objects G332.9457+02.3855 and G338.5459+02.1175 were originally classified as MYSOs, but since the observation date have been found to have too low a luminosity for this to be the case, and are likely lower mass young stellar objects. However, since they both possess strong CO emission we have included them in the final sample and discuss them in Appendix B.

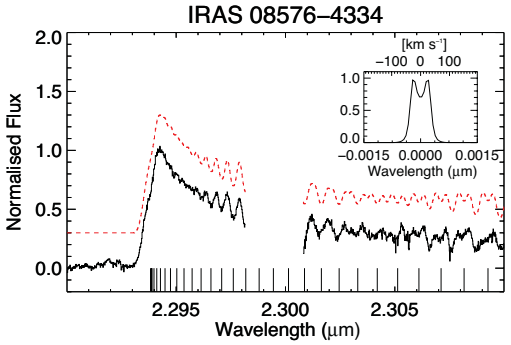

Figure 1. Spectrum of the first overtone bandhead emission of IRAS 08576−4334 (solid black). The gap in the data is due to the spacing between chips three (left) and four (right) of the detector. The best-fitting model is shown above (dashed red) and has been shifted upwards for clarity. The theoretical wavelengths of the transitions that make up the bandhead are marked on the abscissa, and have been shifted to account for relative motion. The panel shows the line shape of the $J = 51$–50 transition that was adopted for the best-fitting model.

Fig. 1 shows the bandhead of IRAS 08576−4334, which is a good example of the CO bandhead feature due to the prominent emission and the high signal-to-noise ratio. Plotted above the data is our final best-fitting model (discussed in Section 3). The inset shows the line shape of the $J = 51$–50 transition that is the result of the best-fitting model, displaying a double peaked profile due to the motion in the disc.

3 MODELLING THE EMISSION

To determine whether the CO emission originates from circumstellar discs and to constrain the physical properties of the emitting region, we compare the observations to a model of emission from a disc. There are several ways in which the physical parameters within the disc can be modelled. For example, Bik & Thi (2004) assume a simple isothermal disc; and Berthoud et al. (2007) assume the surface density and temperature of the disc decrease as power laws. Carr (1989) and Chandler et al. (1995) determine the temperature and density structure by balancing the heating and cooling mechanisms at work on the surface of a thin alpha disc (see Shakura & Sunyaev 1973) which is isothermal in the vertical direction.

To fit the emission using a disc model, we first divide the disc into 75 radial rings each with 75 azimuthal cells. Each cell is assigned a temperature and surface density calculated from the relevant disc description (see Section 3.1). We assume Keplerian rotation for the disc, and the velocity of each cell to the line-of-sight is determined assuming the disc is at an inclination i to the vertical.

Our model of the CO emission is based on Wheelwright et al. (2010), which was in turn based on that of Kraus et al. (2000), and briefly described here. The population of the CO rotational levels, to a maximum of $J = 100$, for the $v = 2$–0 vibrational transition is determined in each cell according to the Boltzmann distribution, which assumes local thermodynamic equilibrium, and a CO/H_2 ratio of 10^{-4}. The intrinsic line shape of each transition is assumed to be Gaussian, with a linewidth of Δv. The intensity of emission is then calculated from the equation

$$I_v = B_v(T)\left(1 - \mathrm{e}^{-\tau_v}\right). \quad (1)$$

The emission from each cell is weighted by its solid angle subtended by the cell on the sky, and wavelength shifted with respect to the line-of-sight velocity due to the rotational velocity of the disc. The emission from all cells is then summed together, smoothed to the instrumental resolution, and shifted in wavelength to account for the radial velocity of the object to produce the entire CO bandhead profile for the disc.

3.1 Disc models

We have investigated the use of three different approaches to model the disc. Here, we discuss their differences.

3.1.1 Model A

Our first model, Model A, is purely analytic in nature (as in Berthoud et al. 2007) and describes the excitation temperature and surface number density as decreasing power laws,

$$T(r) = T_\mathrm{i}\left(\frac{r}{R_\mathrm{i}}\right)^p \quad (2)$$

$$N(r) = N_\mathrm{i}\left(\frac{r}{R_\mathrm{i}}\right)^q, \quad (3)$$

where T_i and N_i are the excitation temperature and surface density at the inner edge of the disc R_i, and p and q are the exponents describing the temperature and surface density gradient, respectively. The optical depth, τ, is taken to be the product of the absorption coefficient per CO molecule, and the CO column density. Since we are considering a geometrically thin disc, the column density is given by the surface number density N.

3.1.2 Model B

Our second model, Model B, is based on balancing the heating and cooling descriptions of a disc as in Carr (1989), later updated by Chandler et al. (1995). The disc is assumed to be dominated by stellar heating, with a contribution from heating via viscosity, and thus the temperature considered is the surface temperature of the disc. The disc is assumed to be steady state, and thus has a constant accretion rate throughout. The disc is under local thermodynamic equilibrium. Finally, the disc is isothermal in the vertical direction, and is heated via absorption of the stellar radiation field and the conversion of gravitational potential energy into thermal energy via viscosity. The viscosity within the disc is described by the alpha prescription (Shakura & Sunyaev 1973). The mass accretion rate of MYSOs is expected to be high (up to 10^{-3} $\mathrm{M_\odot\,yr^{-1}}$) and the discs are likely turbulent; therefore we adopt a value of $\alpha = 1.0$, corresponding to a highly viscous disc environment.

To obtain the excitation temperature and surface number density at a certain radius within the disc, we balance the heating and cooling rates at the disc surface. This condition is then iterated through with increasing temperatures until fulfilled, and the final physical properties are adopted for the particular radius. This is repeated throughout the disc.

3.1.3 Model C

Our third model, Model C, is again based on balancing the heating and cooling mechanisms of a disc, but as described in Vaidya, Fendt & Beuther (2009). In this disc, the heating via viscosity is assumed to dominate the temperature structure, and as such the temperature here can be considered the midplane temperature of the disc. The disc is steady state and we again adopt $\alpha = 1.0$.

We again balance the heating and cooling rates, which provides the temperature and number density at a specific radius within the disc via iteration. The heating due to irradiation from the star is not included in this iteration because we are considering the midplane temperature of the disc, but is instead added to the temperature reported from this convergence, yielding the final excitation temperature.

In both Models B and C, the mass accretion rate directly sets the temperature structure throughout the disc. The inner edge of the emission region is set to the radius at which the temperature reaches 5000 K (where we assume CO is destroyed), and the outer edge of the disc is set to where the temperature drops below 1000 K (where we assume CO is no longer ro-vibrationally excited). The optical depth is taken to be $\tau = \kappa\rho H$ where H is the scale height of the disc and κ is the opacity taken from Ferguson et al. (2005).

3.2 The fitting procedure

The best-fitting model is determined using the downhill simplex algorithm, implemented by the AMOEBA routine of the IDL distribution. The input spectra are first continuum subtracted (which is assumed to be linear given the small range in wavelength), and then normalized to the peak of the bandhead emission. Model fits are compared to the data using the reduced chi-squared statistic, χ^2_r, and the error in the data is taken to be the standard deviation of the flux in the pre-bandhead portion of the spectra.

The fitting routine is repeated with six starting positions spread across the parameter space to avoid recovering only local minima in χ^2_r. Table 2 shows the ranges over which we search in parameter space. The stellar mass, radius and effective temperature are fixed

Table 2. Allowed ranges of parameters for the model fitting procedure, for disc Models A, B and C. Note that density refers to the surface number density.

Parameter	Used in	Range
Mass accretion rate $\dot{M}$	B, C	$10^{-7.5} < \dot{M} < 10^{-3.5}$ M$_\odot$ yr^{-1}
Inclination i	A, B, C	$0 < i < 90^\circ$
Intrinsic linewidth Δv	A, B, C	$1 < \Delta v < 30$ km s^{-1}
Inner disc radius R_i	A	$1 < R_i < 100$ R$_\star$
Inner disc temperature T_i	A	$1000 < T_i < 5000$ K
Inner disc density N_i	A	$10^{12} < N_i < 10^{25}$ cm^{-2}
Temperature exponent p	A	$-5 < p < 0$
Density exponent q	A	$-5 < q < 0$

parameters, and are calculated from the bolometric luminosity of each object using interpolation of the main-sequence relationships in Martins, Schaerer & Hillier (2005), unless otherwise stated in Table 1. The free parameters of the fit are, for Model A: the inner disc radius, temperature and surface density R_i, T_i, N_i, the temperature and density exponents p, q, the disc inclination i and the intrinsic linewidth Δv. For Models B and C, the free parameters are: the mass accretion rate $\dot{M}$, disc inclination i and intrinsic linewidth Δv.

3.3 A test of the disc models – W33A

The object G012.9090−00.2607 (hereafter W33A) is a well-known MYSO that has been studied extensively in recent years (de Wit et al. 2010; Wheelwright et al. 2012a), and thus offers a useful check of our models. The work of de Wit et al. (2010) determined the inclination of the system to be $40^\circ < i < 70^\circ$ through modelling of the SED. We have fitted the spectrum of W33A using the three disc models described in Section 3.1 to test which is most applicable to the circumstellar environment of MYSOs. Fig. 2 shows the data and the best fits, and Table 3 shows the best-fitting parameters for each model.

Model A clearly gives the best fit to these data, as can be seen from the reduced chi-squared statistic. All models reproduce the peak of the bandhead and blue side slope well. However, only Model A accurately reproduces the individual line profiles between 2.296 and 2.298 μm with a sufficiently small intrinsic linewidth. Models B and C both have similar chi-squared values, twice that of Model A. Furthermore, the inclination of Model B is too low to agree with de Wit et al. (2010). Model C is more sensitive to high accretion rates, which allows higher temperatures in the disc to be reached. As can be seen, higher mass accretion rates are reported than in Model B. The hotter disc means that the CO emission region is located further out in the disc, and therefore suffers from less rotational broadening. This is why Model C reports a higher inclination. However, this is still too low to be consistent with de Wit et al. (2010).

Model A provides additional parameters in the temperature and density exponents, and their respective values at the inner edge of the CO emission region. This allows us to effectively change the amount of material within the disc, and provides a better fit to these data. While Models B and C are both based on physical descriptions of accretion discs, they may not contain all of the relevant details. For example, these models also assume emission from a flat disc, but in reality different disc geometries may need to be considered, such as flared discs, or discs with discrete vertical layers. For this reason, we chose to adopt disc Model A as a basis for the fitting routine for the other MYSOs, as it allows freedom to account for different emission geometries and is not reliant upon possibly inaccurate assumptions regarding the temperature and density structure of these discs.

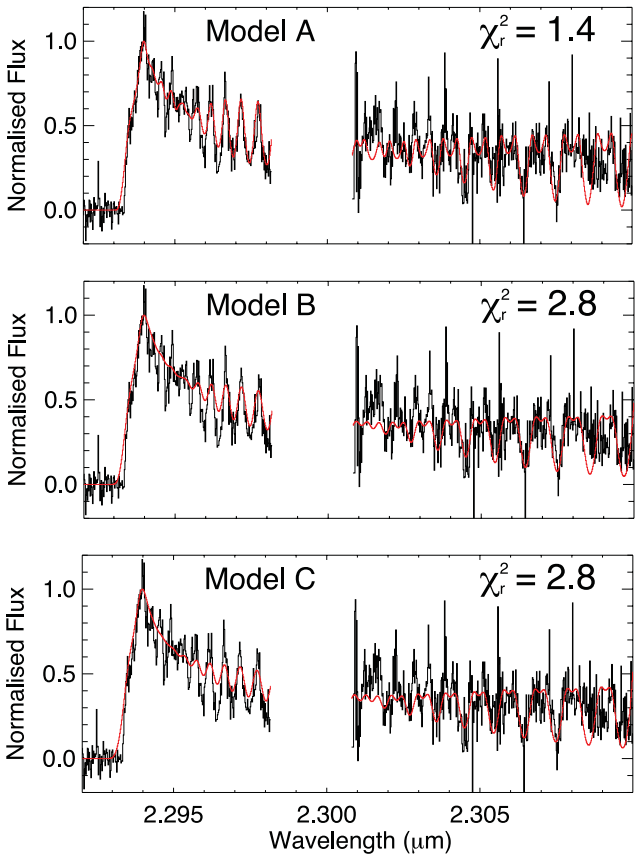

Figure 2. Best-fitting models to G012.9090−00.2607 (W33A) using each disc model. Best-fitting parameters are shown in Table 3. Model A provides the best fit as can be seen from the reduced chi squared statistic. Models B and C struggle to reproduce the peak to trough variation seen in the spectrum between 2.296 and 2.298 μm. All models struggle to fit the initial data points on chip four.

Table 3. Best-fitting parameters using disc Models A, B and C for the spectrum of G012.9090−00.2607 (W33A).

Disc model	$\dot{M}$ (M$_\odot$ yr^{-1})	Δv (km s^{-1})	i ($^\circ$)	χ^2_r
A	–	21	37	1.4
B	7.76×10^{-6}	29	13	2.8
C	2.14×10^{-5}	29	27	2.8

Adopting disc Model A, fits to all objects were obtained as described in Section 3.2. The errors were calculated by holding all but one parameters constant at their best-fitting value, and varying the selected parameter until the difference in χ^2_r was equal to one. For some parameters, the 1-sigma error values were beyond the range of allowed parameters for our fitting routine. For all objects, we attempted the fitting procedure using data from both chips three and four of the detector. If a satisfactory fit was not obtained, we limited the wavelength range of fitting to only include data from chip three and repeated the fitting procedure. Tests with individual objects showed that extrapolation of a fit using only the wavelength range of chip three, on to chip four, produced similar results to a fit involving both chips. This can be seen in several objects (e.g.

G296.2654−00.3901 and M8E-IR) where the extrapolated fit across chip four is consistent with the location of the rotational lines that were not included in the fitting range due to a poor signal-to-noise ratio at these wavelengths.

4 FULL SAMPLE RESULTS

We are able to fit all objects with spectra that have sufficiently strong CO emission, found to be above approximately six times the rms noise in the pre-bandhead section of the spectrum. We fit eight MYSOs and the two lower mass YSOs across the full chip three and four wavelength range, and also use only chip three (or a portion of chip three) to fit the remaining nine MYSOs. Three objects (G293.8947−00.7825, G332.0939−00.4206 and G339.6816−01.2058) were determined to have CO emission that was too weak, or a signal-to-noise ratio that was too low, to provide a reliable fit, but for completeness we include their spectra in Appendix B. The two reclassified low-mass YSO objects, G332.9457+02.3855 and G338.5459+02.1175, are excluded from our analysis here and discussed in Appendix B.

Figs 3 and 4 present the spectra and best-fitting models using disc Model A to each of the MYSOs with CO emission. Objects where only chip three has been used for the fitting routine are indicated with a greyed-out chip four region. Table 4 shows the best-fitting model parameters for each of the objects, with associated 1-sigma errors. Errors marked with an asterisk should be considered lower limits, as the full 1-sigma error value was beyond our allowed parameter range.

In general, across the seven objects whose inclinations have been constrained before, our best-fitting parameters agree with the previous results, within error margins. Comments and comparisons on an object by object basis are presented in Appendix A. The majority of objects have discs beginning within a few astronomical units of the stellar surface, and inner disc temperatures close to the dissociation temperature of CO (5000 K). The distribution of the inner surface densities of the disc has a geometric average of $\bar{N}_{\rm i} = 5.5 \pm 8 \times 10^{20}\,{\rm cm}^{-2}$. It should be noted that even though CO should be dissociated by stellar UV flux at these small distances, we find as in Bik & Thi (2004) and Wheelwright et al. (2010) that the density is sufficient for self-shielding to occur ($N > 10^{15}{\rm cm}^{-2}$; van Dishoeck & Black 1988).

Fig. 5 shows the distribution of the best-fitting inclinations and the temperature and density exponents of the MYSOs. While our inclinations are consistent with most previously published data for objects, IRAS 08576−4334 is not, and we discuss this in detail in Appendix A. The distribution of the best-fitting inclinations is essentially consistent with the inclinations being random ($i = 60^\circ$), as the mean inclination value is $\bar{i} = 55 \pm 25^\circ$. The temperature gradients are skewed towards higher values, but have a mean of $\bar{p} = -0.6 \pm 0.5$, close to the -0.75 suggested for a flat accretion disc. We note that two objects show well-constrained temperature gradients of -0.43, which are consistent with flared, irradiated discs (Chiang & Goldreich 1997). The surface density gradients are more evenly spread across the parameter space, with a mean of $\bar{q} = -1.5 \pm 1.2$. This is consistent with the surface density gradient for a flat accretion disc, although it is associated with a large error. The average intrinsic linewidth of the fits is $\bar{\Delta\nu} = 20 \pm 12\,{\rm km\,s}^{-1}$. Apart from two objects (G287.3716+00.6444 and IRAS 17441−2910) the linewidths are approximately 10 times the thermal linewidths expected for CO between 1000 and 5000K, suggesting that the emitting material is dominated by macro-turbulent motions or infall.

5 DISCUSSION

5.1 Disc sizes – the location of the emission

We find a range of disc sizes from our results. However, in the majority of cases, the inner edge of the CO emission region is within a few au. The outer edge of the emission region varies much more, giving rise to three very large discs. However, the objects with very large discs have temperature exponents that are poorly constrained. This allows very shallow gradients (as can be seen in Fig. 6), which in turn produce large outer disc radii, because this is defined as where the excitation temperature drops below 1000 K. Thus, these large disc sizes are likely not physical and much smaller discs can be produced with an exponent that is still within the uncertainty in the best-fitting value.

To compare the location of the CO emission to the circumstellar disc as a whole, we can calculate the dust sublimation radius, $R_{\rm S}$, in au for each object:

$$R_{\rm S} = 1.1\sqrt{Q_{\rm R}}\left(\frac{L_\star}{1000\,{\rm L}_\odot}\right)^{0.5}\left(\frac{T_{\rm S}}{1500\,{\rm K}}\right)^{-2}, \quad (4)$$

where $Q_{\rm R}$ is the ratio of absorption efficiencies of the dust, and $T_{\rm S}$ is the temperature at which the dust sublimates (Monnier & Millan-Gabet 2002). We take $Q_{\rm R} = 1$ and $T_{\rm S} = 1500$ K. This is then compared to both the inner and outer radii of the CO emission disc from our model fits. Fig. 6 shows histograms of the ratios between these quantities.

As expected, we find that the majority of objects, approximately 75 per cent, have CO discs whose inner extent is less than the dust sublimation radius. Approximately 30 per cent have CO discs with an outer extent below the dust sublimation radius. However this percentage is increased if we exclude the artificially large discs discussed earlier. Concerning the remaining object, there are several cases where the inner and/or outer disc radii are only a few times larger than the dust sublimation radius. Our treatment of the sublimation is simplistic. Factors such as rapid accretion rates, backwarming and non-homogeneous dust grain sizes may increase the dust sublimation radius to several times the value we predict. Therefore, the best-fitting disc properties appear consistent with physical expectations. Consequently, we suggest that, in general, the best-fitting discs can be associated with gaseous accretion discs that are close to the central star. As this is the largest sample of MYSOs with CO bandhead emission studied to date, this provides strong evidence for the existence of small-scale accretion discs around these objects.

5.2 Determining mass accretion rates

As we discuss previously, the use of a physical disc model that directly includes the relevant physics needed to determine a mass accretion rate is attractive. However, as these models did not fit our data well, we were unable to find accretion rates directly from the fits. Therefore, we investigated comparing the radial profiles of the temperature and density from our fits to those predicted by an accretion disc (Model C) for $\dot{M} = 10^{-3.5}$ to $10^{-7.5}\,{\rm M}_\odot\,{\rm yr}^{-1}$, in an effort to determine an estimate for the mass accretion rate of each object. We find that, for many of the objects, the mass accretion rates obtained from the temperature profile and the density profile differed by orders of magnitude. Also, several accretion rates were difficult to determine due to very different gradients between our fit and the accretion disc model, and the values obtained are therefore unreliable. On average, we found that the mass accretion rate from

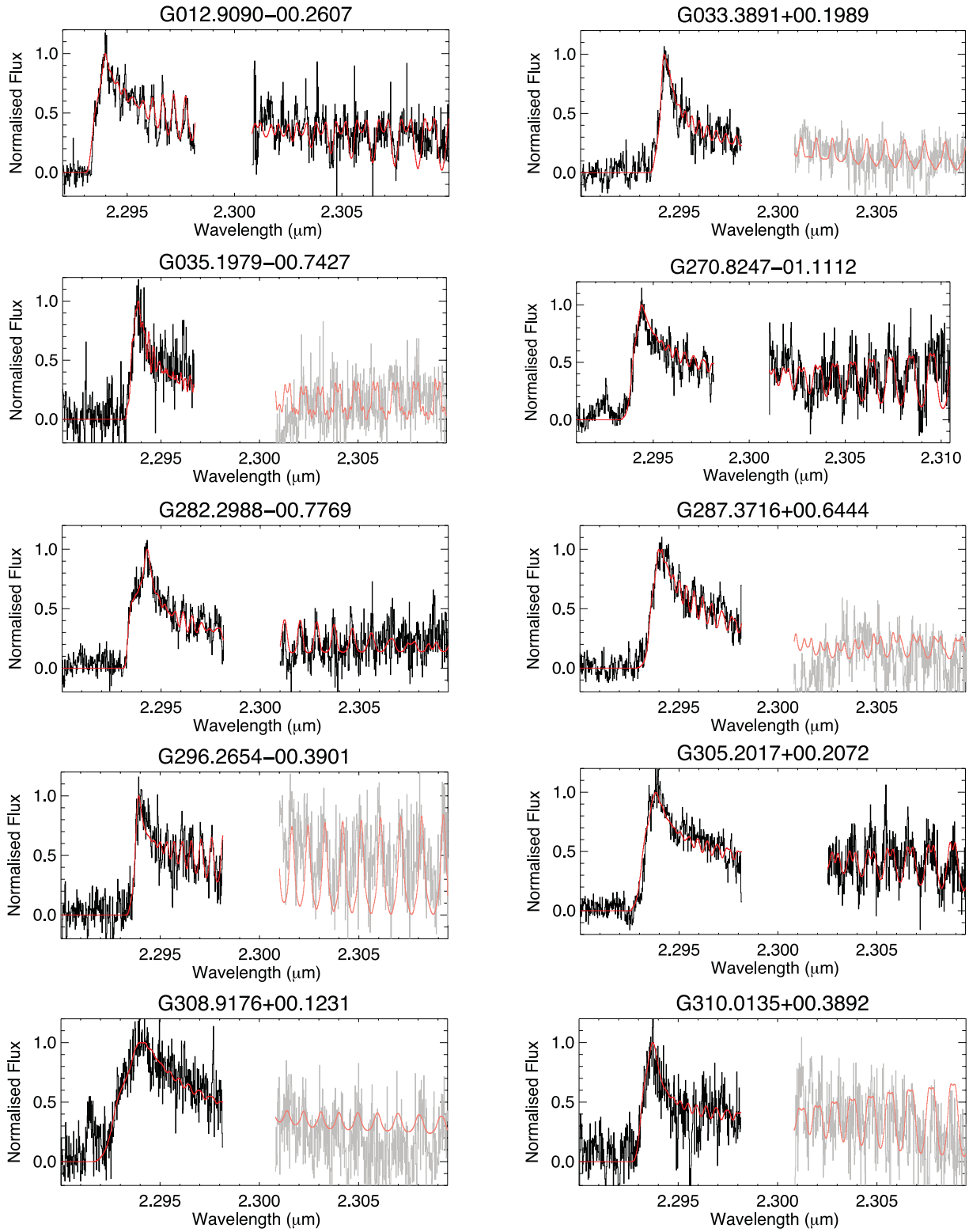

Figure 3. Spectra (black) and model fits (red) to the CO emission of the objects in the sample, using disc Model A. Data that are greyed out are not included in the fitting procedure because of poor quality, but have been included for completeness. For G035.1979−00.7427 and G305.2017+00.2072, small ranges of the spectrum at the edges of the detectors were removed because of excessive noise in the data.

the temperature gradients suggested $\dot{M} > 10^{-4}\,\mathrm{M}_{\odot}\,\mathrm{yr}^{-1}$ while the surface density distribution suggested $\dot{M} < 10^{-7}\,\mathrm{M}_{\odot}\,\mathrm{yr}^{-1}$.

We conclude that our model fits cannot currently be used to determine the mass accretion rates of MYSOs. While this has been performed in previous studies of lower mass young stellar objects (Carr 1989; Chandler et al. 1995), the higher resolution of our data demonstrates that there are many rotational lines that cannot be fitted using these simple disc models. These models may

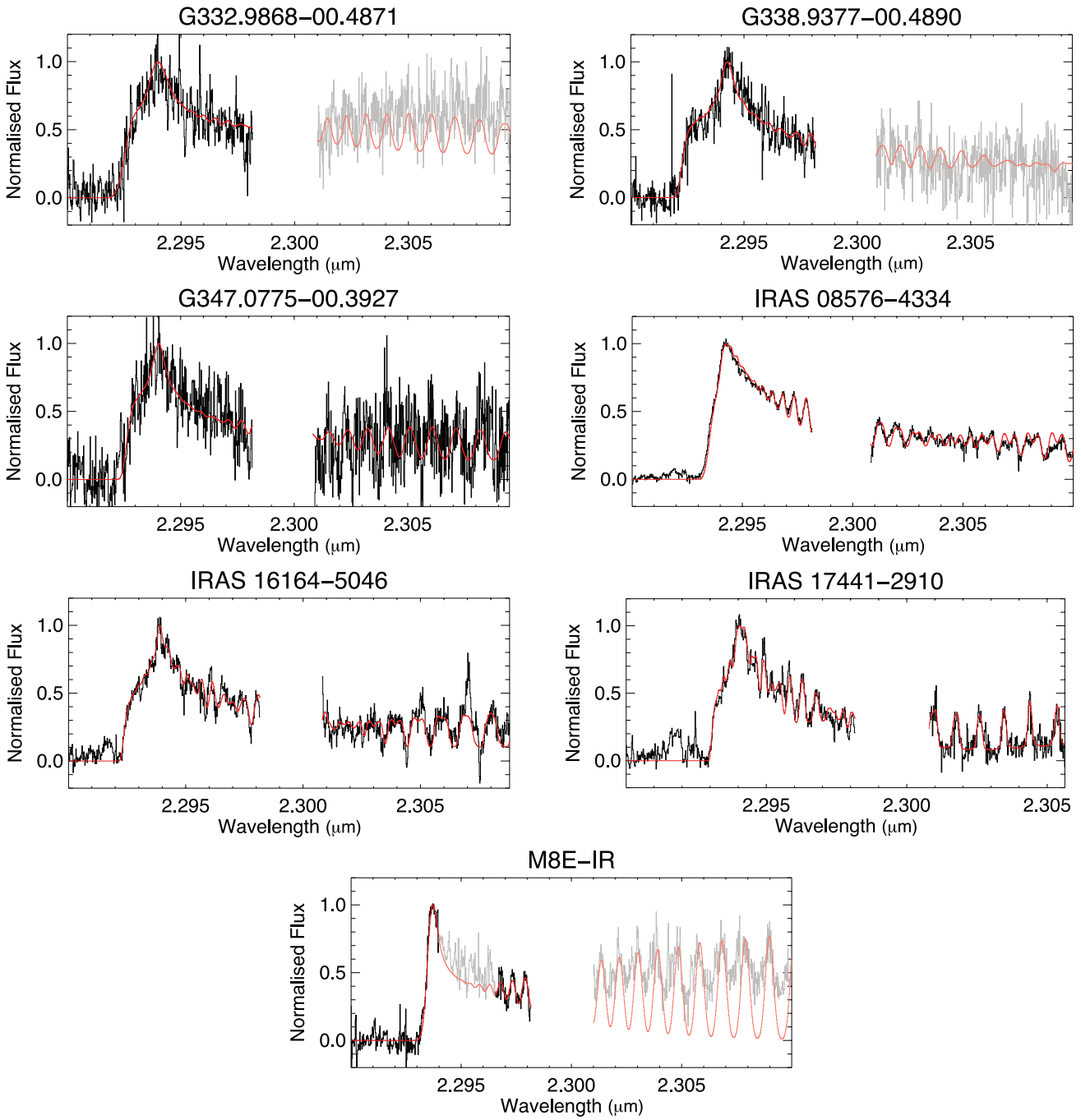

Figure 4. Spectra (black) and model fits (red) to the CO emission of the objects in the sample, using disc Model A. Data that are greyed out are not included in the fitting procedure because of poor quality, but have been included for completeness. The range of fitting for M8E-IR was restricted to obtain a good fit (see Appendix A for full discussion). For IRAS 17441−2910, the portion of the spectrum beyond 2.306 μm was not used because an artificial drop in flux was caused by the detector.

be inadequate in accurately representing the physical situation that gives rise to CO bandhead emission from discs with high accretion rates. Also, the study of only a single bandhead may not offer sufficient information to reliably determine the physical properties of discs and thus cannot accurately constrain mass accretion rates in this way. Observations covering a larger range in wavelength, for instance with VLT/XSHOOTER, would allow fitting of additional bandheads that probe different temperature regimes, at the expense of the high spectral resolution employed in this paper.

5.3 Are these typical MYSOs?

In this section we consider whether the MYSOs with CO emission differ from those without. An important question since the detection rate of CO emission in the spectra of MYSOs is approximately 25 per cent.

MYSOs are typically red objects with a featureless continuum in the optical and NIR, so we cannot accurately constrain their stellar properties such as effective temperature and radius. Therefore, we investigate whether the parameters of the best-fitting models display

Table 4. Quantities used for the model fitting, and results. The stellar mass, radius and effective temperature are derived from bolometric luminosity using interpolation from the main sequence relationships described in Martins et al. (2005), unless otherwise stated. The outer disc radius is defined at the point in the disc in which the temperature drops below 1000 K, so no error is presented. If an error value is marked with an asterisk, the change in the value of the reduced chi-squared statistic χ^2_r was less than one across the allowed parameter range.

Object	$M_\star$ ($M_\odot$)	$R_\star$ ($R_\odot$)	$T_{\rm eff}$ (K)	$R_{\rm i}$ (au)	$R_{\rm o}$ (au)	$T_{\rm i}$ (K)	$N_{\rm i}$ ($\rm cm^{-2}$)	p	q	i (°)	Δv ($\rm km\,s^{-1}$)	χ^2_r
MYSOs												
G012.9090−00.2607	21.2	7.0	33500	$2.3^{+0.9[d]}_{-1.0}$	76	2300^{+50}_{-480}	$2.2^{+40}_{-d} \times 10^{21}$	$-0.25^{+0.25[d]}_{-4.75[d]}$	$-4.10^{+1.80}_{-0.90[d]}$	37^{+16}_{-11}	$21.0^{+9.0[d]}_{-16}$	1.4
G033.3891+00.1989	12.3	4.8	26500	$2.1^{+0.1[d]}_{-1.0}$	3200	$4600^{+400[d]}_{-1800}$	$0.4^{+7}_{-d} \times 10^{21}$	$-0.06^{+0.06[d]}_{-4.94[d]}$	$-1.70^{+0.30}_{-3.30[d]}$	$40^{+50[d]}_{-25}$	$29.0^{+1.0[d]}_{-17}$	2.8
G035.1979−00.7427	17.7	6.1	31200	$2.3^{+0.5[d]}_{-2.0}$	440	$3100^{+10}_{-3100[d]}$	$1.4^{+d}_{-d} \times 10^{23}$	$-0.20^{+0.20[d]}_{-4.80[d]}$	$-4.00^{+1.40}_{-1.00[d]}$	$36^{+54[d]}_{-20}$	$2.9^{+10}_{-2.9[d]}$	1.8
G270.8247−01.1112	12.3	4.8	26500	$1.1^{+0.5[d]}_{-1.0}$	93	3600^{+10}_{-960}	$0.4^{+1.9}_{-0.4} \times 10^{22}$	$-0.32^{+0.10}_{-0.20}$	$-1.60^{+0.40}_{-0.70}$	$89^{+1[d]}_{-40}$	$18.9^{+21.1[d]}_{-13}$	2.8
G282.2988−00.7769	11.8	4.7	26100	$1.7^{+0.5[d]}_{-0.6}$	9	4800^{+10}_{-1500}	$0.1^{+2.3}_{-d} \times 10^{21}$	$-0.97^{+0.60}_{-2.20}$	$-1.40^{+1.40[d]}_{-3.60[d]}$	$80^{+10[d]}_{-30}$	$16.3^{+13.7[d]}_{-16.3[d]}$	2.8
G287.3716+00.6444	17.1	6.0	30800	$0.1^{+0.1}_{-0.1}$	3	4200^{+80}_{-720}	$9.1^{+d}_{-4.2} \times 10^{24}$	$-0.45^{+0.10}_{-0.10}$	$-0.88^{+0.88[d]}_{-0.10}$	17^{+4}_{-2}	$3.1^{+1.2}_{-0.6}$	7.1
G296.2654−00.3901	9.6	4.0	23600	$1.7^{+0.2[d]}_{-1.0}$	530	3400^{+60}_{-1280}	$0.1^{+3.1}_{-0.0} \times 10^{23}$	$-0.20^{+0.20[d]}_{-0.40}$	$-2.20^{+0.90}_{-0.80}$	$23^{+67[d]}_{-23[d]}$	$28.0^{+2.0[d]}_{-22}$	1.3
G305.2017+00.2072	20.4	6.8	33100	$0.6^{+0.3}_{-0.3}$	52	2930^{+20}_{480}	$2.1^{+1.6}_{-1.7} \times 10^{21}$	$-0.27^{+0.10}_{-0.10}$	$-1.61^{0.20}_{-0.40}$	43^{+13}_{-8}	$14.5^{+15.5[d]}_{-8}$	4.7
G308.9176+00.1231	31.7	9.0	37400	$0.7^{+1.6}_{-0.6}$	9	4430^{+30}_{-3200}	$4.8^{+d}_{-d} \times 10^{21}$	$-0.59^{+0.20}_{-4.80[d]}$	$-0.14^{+0.14[d]}_{-3.6[d]}$	$67^{+23[d]}_{-38}$	$12.6^{+17.4[d]}_{-12.6[d]}$	0.9
G310.0135+00.3892	21.8	7.0	33800	$2.8^{+0.5[d]}_{-2.0}$	69	3760^{+100}_{-1400}	$3.8^{+10^{21}}_{-d} \times 10^{12}$	$-0.43^{+0.20}_{-4.57[d]}$	$-0.50^{+0.50[d]}_{-4.5[d]}$	$67^{+23[d]}_{-41}$	$25.5^{+4.5[d]}_{-25.5[d]}$	2.0
G332.9868−00.4871	16.6	5.9	30400	$0.5^{+0.8}_{-0.3}$	7	4400^{+120}_{1600}	$0.1^{+1.9}_{-d} \times 10^{21}$	$-0.59^{+0.20}_{-0.4}$	$-0.01^{+0.01[d]}_{-1.3}$	$78^{+12[d]}_{-38}$	$29.7^{+0.3[d]}_{-28}$	1.9
G338.9377−00.4890	7.4	3.4	21400	$0.3^{+0.3}_{-0.2}$	1	$4900^{+100[d]}_{-2200}$	$0.4^{+2.1}_{-d} \times 10^{20}$	$-1.22^{+0.90}_{-3.78[d]}$	$-1.63^{+1.63[d]}_{-3.37[d]}$	$89^{+1[d]}_{-45}$	$29.9^{+0.1[d]}_{-29.9[d]}$	1.2
G347.0775−00.3927	7.0	3.3	20900	$0.4^{+1.1[d]}_{-0.3}$	3	4600^{+10}_{-2000}	$0.3^{+4.7}_{-d} \times 10^{21}$	$-0.79^{+0.60}_{-4.21[d]}$	$-1.14^{+1.14[d]}_{-3.86[d]}$	$84^{+6[d]}_{-61}$	$26.5^{+3.5[d]}_{-26.5[d]}$	1.9
IRAS 08576−4334	6.1[c]	3.0	19200	$0.6^{+0.1}_{-0.1}$	7	$4980^{+20[d]}_{-800}$	$2.8^{+6.4}_{-6.4} \times 10^{21}$	$-0.71^{+0.05}_{-0.05}$	$-0.001^{+0.001[d]}_{-0.60}$	$65^{+4.1}_{-11}$	$15.7^{+2.4}_{-3}$	2.9
IRAS 16164−5046	34.9	9.8	38300	$1.9^{+0.1}_{-0.1}$	5	4380^{+10}_{-1900}	$0.1^{+2.1}_{-d} \times 10^{22}$	$-1.45^{+0.90}_{-3.55[d]}$	$-1.37^{+1.37[d]}_{-3.63[d]}$	62^{+16}_{-12}	$11.9^{+18.1[d]}_{-8}$	1.7
IRAS 17441−2910	56.9	14.3	41300	$6.0^{+0.6[d]}_{-0.1}$	13	3880^{+10}_{-400}	$3.8^{+0.2}_{-d} \times 10^{21}$	$-1.72^{+1.30}_{-0.10}$	$-1.00^{+1.00[d]}_{-4.00[d]}$	53^{+2}_{-16}	$3.7^{+0.6}_{-3.7[d]}$	0.6
M8E-IR[e]	13.5[b]	5.1	27800	$1.5^{+0.9[d]}_{-0.4}$	54	2300^{+10}_{-320}	$0.2^{+10}_{-d} \times 10^{20}$	$-0.24^{+0.24[d]}_{-4.76[d]}$	$-2.16^{+1.1}_{-2.84[d]}$	$14^{+10}_{-14[d]}$	$49^{+11[d]}_{-13}$	2.1
Non-MYSOs (see Appendix B)												
G332.9457+02.3855[a]	0.5	3.0	5000	$0.7^{+0.7[d]}_{-0.6}$	4	3240^{+10}_{-880}	$2.5^{+5.3}_{-d} \times 10^{20}$	$-0.73^{+0.73[d]}_{-4.27[d]}$	$-2.60^{+2.60[d]}_{-2.40[d]}$	$66^{+24[d]}_{-66[d]}$	$29.8^{+0.2[d]}_{-29.8[d]}$	2.7
G338.5459+02.1175[a]	0.5	3.0	5000	$1.2^{+0.2[d]}_{-0.4}$	61	$5000^{+0[d]}_{-1000}$	$1.5^{+6.0}_{-0.9} \times 10^{22}$	$-0.36^{+0.00}_{-0.20}$	$-3.77^{+1.40}_{-1.23[d]}$	$87^{+3[d]}_{-61}$	$28.4^{+1.6[d]}_{-11}$	3.9

[a]Originally thought to be an MYSO prior to observations, but subsequent analysis showed that the bolometric luminosity is too low for this to be the case. The stellar mass, radius and effective temperature of these objects are therefore estimated from typical T Tauri star values (Covey et al. 2011).
[b]Taken from Linz et al. (2009), which is based on the best-fitting model from Robitaille et al. (2007).
[c]Determined from the position in the K versus $J-K$ diagram of Bik et al. (2006), as in Wheelwright et al. (2010).
[d]The value of χ^2_r did not change by one over the allowed parameter range.
[e]The wavelengths fitted and ranges of allowed fit parameters were altered to obtain a good fit (see text for details).

a pattern which may explain why only some MYSOs exhibit this emission. In particular, it is conceivable that for CO emission to be observed, the inclination of the disc is required to be close to face on. However, the inclinations of the objects are spread relatively evenly between 0° and 90°, with a slight preference for higher inclinations, suggesting this is not the case. In addition, we note that the average bolometric luminosity of our sample of objects with CO emission is $5 \times 10^4\,L_\odot$, which is typical of objects within the RMS survey. Therefore, we conclude that the properties of the MYSOs that exhibit CO bandhead emission do not indicate what specific geometry and/or conditions result are required for the presence of this emission.

Consequently, it is not certain why the presence of CO bandhead emission is not ubiquitous in the spectra of MYSOs. It is possible that the objects with CO emission represent a different evolutionary stage of MYSOs than those without. It is difficult to test this hypothesis. As an initial test, we investigate the infrared colours of the observed MYSOs, which are likely affected by key factors such as circumstellar geometries on astronomical unit scales, inclination and envelope mass/infall rate. To determine whether the MYSOs with CO bandhead emission appear representative of MYSOs in general or are a specific subset of MYSOs, we compared their NIR colours with those of approximately 70 objects from the RMS data base, which we show in the upper panel of Fig. 7. To ensure a valid comparison with our objects, the control sample was selected to have a high luminosity ($L > 10^4\,L_\odot$) and be bright in the K band ($K < 10$ mag). We compared the $J-K$ and $H-K$ colours of the two samples with the Kolmogorov–Smirnov (KS) test and found that the hypothesis that the NIR colours of the MYSOs with CO bandhead emission are drawn from the distribution of NIR colours exhibited by the RMS population cannot be discounted with any significance. The objects observed to have CO bandhead emission are generally bright in the K band. However, this is a selection effect and does not imply that only objects with such emission are intrinsically brighter in the K band.

We also examined the mid-infrared (MIR) colours of the sample. Specifically, we compared the *MSX* ($F_{21\,\mu m} - F_{8\,\mu m}$), ($F_{21\,\mu m} - F_{12\,\mu m}$) and ($F_{21\,\mu m} - F_{14\,\mu m}$) colours of the objects with CO bandhead emission to the RMS population mentioned earlier. The lower panel of Fig. 7 shows the cumulative distribution of the

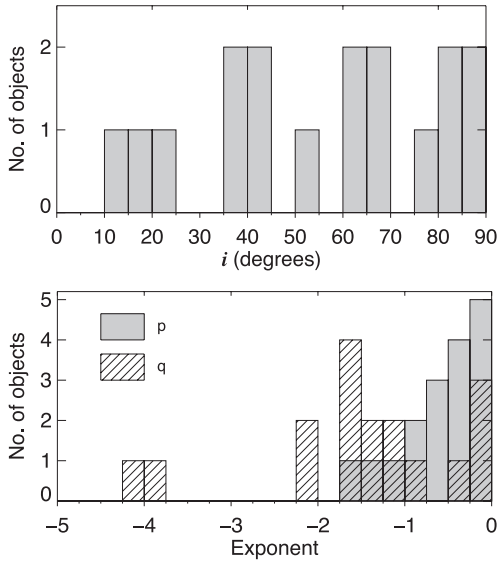

Figure 5. Distributions of inclinations (top), and temperature and surface density exponents (p and q, respectively, bottom) determined from the fits to the 17 MYSOs with detected CO bandhead emission.

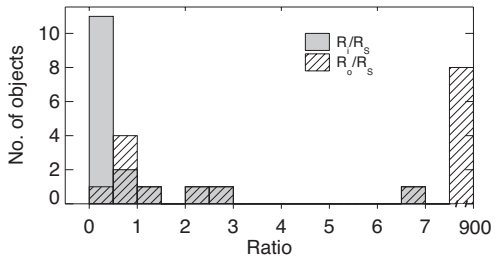

Figure 6. Ratio of inner and outer CO disc radii, R_i, R_o, compared to the dust sublimation radius R_S for each object. The majority of objects have inner radius well below the dust sublimation radius, and in some cases the entire CO disc is inside the sublimation radius. Most of the discs are within a few dust sublimation radii. Note that the final bin in the histogram is uneven and extends from 7.5 to 900.

($F_{21\,\mu m} - F_{8\,\mu m}$) colours. Using the KS test, we found that the hypothesis that the MIR colours of the objects with CO emission are drawn from the total RMS distribution of MIR colours cannot be discounted with any significance. Therefore, the objects with and without CO emission appear no different in terms of both their NIR and MIR colours, suggesting these objects are representative of the RMS population as a whole.

It is therefore unclear from this analysis why only some MYSOs possess CO emission. It has been predicted that models of circumstellar discs of MYSOs can be unstable (Krumholz, Klein & McKee 2007) and that the accretion rate in these discs is not constant (Kuiper et al. 2011). Unstable discs may disrupt the circumstellar material and lead to physical conditions in which CO ro-vibrational emission no longer occurs. If the disc accretion rate is high, this will increase the mid-plane temperature of the disc and move the CO emission region further away from the central protostar, possibly into the surrounding envelope, which may cause the emission to cease. However, without a method to determine the accretion rate of these objects, this hypothesis is difficult to test.

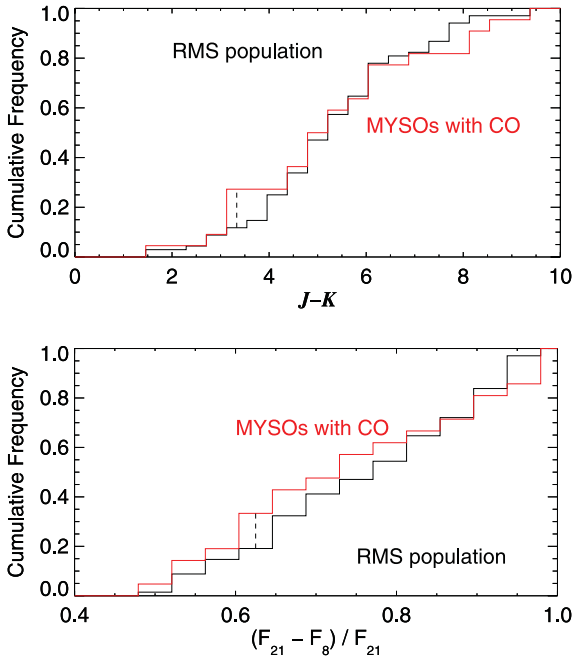

Figure 7. Cumulative frequency of the NIR $J - K$ and normalized MIR ($F_{21\,\mu m} - F_{8\,\mu m}$) colours of the MYSOs with CO emission and the RMS population. The dashed vertical lines indicate the largest deviation between the distributions. Similar distributions were found for the $H - K$, ($F_{21\,\mu m} - F_{12\,\mu m}$) and ($F_{21\,\mu m} - F_{14\,\mu m}$) colours.

5.4 Discs and massive star formation

The physical processes occurring during massive star formation are still not well understood. It is thought accretion proceeds through circumstellar discs at high rates, which are believed to affect the state of the central protostar (Hosokawa & Omukai 2009; Hosokawa, Yorke & Omukai 2010). Furthermore, recent simulations indicate that high accretion rates result in massive discs and that gravitational torques in such self-gravitating discs provide a mechanism to transport angular momentum outwards (Kuiper et al. 2011). Therefore, it is becoming apparent that accretion discs play a central role in the formation of massive stars. However, it is difficult to confirm this observationally. In most cases, the large distances to MYSOs, and their embedded nature, prevent detections of astronomical unit scale circumstellar discs (the exception being IRAS 13481; see Kraus et al. 2010). In some cases, high infall rates have been detected towards massive star-forming regions (see e.g. Beuther, Linz & Henning 2012; Herpin et al. 2012; Qiu et al. 2012; Wyrowski et al. 2012). However, these observations probe scales of approximately 1000 au and larger. Therefore, it is difficult to establish that this material will be accreted by a single object. Consequently, our observational overview of massive star formation is still incomplete.

With this in mind, we note that our sample constitutes the largest sample of MYSOs with CO bandhead emission studied to date (several times that of Wheelwright et al. 2010). Therefore, by confronting the observations with a kinematic model, we can conduct an extensive investigation into the circumstellar environment of these objects. We demonstrate that all the observed bandhead profiles can be successfully fitted with a model of a circumstellar disc in Keplerian rotation. In addition, we have shown that essentially all these models can be associated with gaseous discs interior to the dust sublimation radii of these objects. Finally, we demonstrate that the objects in question appear no different to the ensemble of objects in

the RMS catalogue, the largest most complete catalogue of MYSOs to date. Therefore, the fact that the CO bandhead emission of all the objects observed can be fitted with a disc model supports the scenario in which all MYSOs are surrounded by accretion discs. With our limited wavelength coverage, we were not able to establish precise constraints on the accretion rates. Nonetheless, we find that the disc properties are consistent with high accretion rates. Therefore, these observations are entirely consistent with the hypothesis that MYSOs are massive stars in the process of forming that accrete matter through circumstellar discs.

6 CONCLUSIONS

In this paper we have presented the NIR spectra of 20 MYSOs that possess CO first overtone bandhead emission, the largest sample studied in this way to date. We have fit the spectra of these objects with a model of emission originating in a circumstellar disc in Keplerian rotation. We tested three approaches to describing the properties of such circumstellar discs and found that the spectra were best fit by using an analytic approach to describe the temperature and density within the disc. Our main findings are as follows.

(i) All spectra are well fit by a model of a Keplerian rotation disc.

(ii) The best-fitting disc parameters are consistent with previously published information. The inclinations are spread across a wide rage of angles. The best-fitting temperature and density exponents are, on average, consistent with flat circumstellar discs (subject to some scatter), a handful of objects have exponents consistent with flared, irradiated discs.

(iii) Essentially all the best-fitting discs are located close to the dust sublimation radius, which is consistent with the existence of small-scale gaseous accretion discs around these objects.

We found that the mass accretion rates of the objects are not easily determined from examination of the disc structure as traced by a single CO bandhead. The analysis of further bandheads may allow these accretion rates to be determined. Our high spectral resolution observations of the CO emission of a substantial number of MYSOs and our modelling of this emission are entirely consistent with the scenario in which MYSOs are surrounded by small-scale (<100 au) accretion discs. The objects observed constitute a large sample of circumstellar discs around MYSOs and provide promising targets for future observations and inspiration for detailed modelling of the accretion environment of such objects.

ACKNOWLEDGMENTS

We would like to thank Bhargav Vaidya for useful discussions regarding the physical disc models, and the anonymous referee whose thorough comments helped us to improve the paper. JDI and LTM gratefully acknowledge studentships from the Science and Technology Facilities Council of the United Kingdom (STFC). HEW acknowledges the financial support of the MPIfR in Bonn. This paper has made use of information from the RMS survey data base at http://www.ast.leeds.ac.uk/RMS which was constructed with support from the STFC.

REFERENCES

Berthoud M. G., Keller L. D., Herter T. L., Richter M. J., Whelan D. G., 2007, ApJ, 660, 461
Beuther H., Linz H., Henning T., 2012, A&A, 543, A88
Bik A., Thi W. F., 2004, A&A, 427, L13
Bik A., Kaper L., Waters L. B. F. M., 2006, A&A, 455, 561
Blum R. D., Barbosa C. L., Damineli A., Conti P. S., Ridgway S., 2004, ApJ, 617, 1167
Boley P., Linz H., van Boekel R., Bouwman J., Henning T., Sobolev A., 2012, A&A, 547, 88
Brand J., Blitz L., 1993, A&A, 275, 67
Bronfman L., Nyman L.-A., May J., 1996, A&AS, 115, 81
Carr J. S., 1989, ApJ, 345, 522
Carrasco-González C. et al., 2012, ApJ, 752, L29
Chandler C. J., Carlstrom J. E., Scoville N. Z., 1995, ApJ, 446, 793
Chiang E. I., Goldreich P., 1997, ApJ, 490, 368
Chini R., Neckel T., 1981, A&A, 102, 171
Clarke A. J., 2007, PhD thesis, University of Leeds
Cooper H., MNRAS, submitted
Covey K. R. et al., 2011, AJ, 141, 40
Davies B., Lumsden S. L., Hoare M. G., Oudmaijer R. D., de Wit W.-J., 2010, MNRAS, 402, 1504
de Wit W. J., Hoare M. G., Oudmaijer R. D., Lumsden S. L., 2010, A&A, 515, A45
Egan M. P., Price S. D., Kraemer K. E., 2003, BAAS, 35, 1301
Ellerbroek L. E., Kaper L., Bik A., de Koter A., Horrobin M., Puga E., Sana H., Waters L. B. F. M., 2011, ApJ, 732, L9
Ferguson J. W., Alexander D. R., Allard F., Barman T., Bodnarik J. G., Hauschildt P. H., Heffner-Wong A., Tamanai A., 2005, ApJ, 623, 585
Herpin F. et al., 2012, A&A, 542, A76
Hosokawa T., Omukai K., 2009, ApJ, 691, 823
Hosokawa T., Yorke H. W., Omukai K., 2010, ApJ, 721, 478
Jiménez-Serra I., Martín-Pintado J., Rodríguez-Franco A., Chandler C., Comito C., Schilke P., 2007, ApJ, 661, L187
Kaeufl H.-U., Ballester P., Biereichel P., Delabre B., Donaldson R., Dorn R., Fedrigo E., Finger, 2004, in Moorwood A. F. M., Iye M., eds, Ground-based Instrumentation for Astronomy, SPIE Conf. Ser. Vol. 5492, p. 1218
Kahn F. D., 1974, A&A, 37, 149
Klaassen P. D., Wilson C. D., Keto E. R., Zhang Q., Galván-Madrid R., Liu H.-Y. B., 2011, A&A, 530, A53
Kraus M., Krügel E., Thum C., Geballe T. R., 2000, A&A, 362, 158
Kraus S. et al., 2010, Nat, 466, 339
Krumholz M. R., Klein R. I., McKee C. F., 2007, ApJ, 665, 478
Krumholz M. R., Klein R. I., McKee C. F., Offner S. S. R., Cunningham A. J., 2009, Sci., 323, 754
Kuiper R., Klahr H., Beuther H., Henning T., 2010, ApJ, 722, 1556
Kuiper R., Klahr H., Beuther H., Henning T., 2011, ApJ, 732, 20
Larson R. B., Starrfield S., 1971, A&A, 13, 190
Linz H. et al., 2009, A&A, 505, 655
Lumsden S. L., Hoare M. G., Oudmaijer R. D., Richards D., 2002, MNRAS, 336, 621
Martin S. C., 1997, ApJ, 478, L33
Martins F., Schaerer D., Hillier D. J., 2005, A&A, 436, 1049
Molinari S., Brand J., Cesaroni R., Palla F., 1996, A&A, 308, 573
Monnier J. D., Millan-Gabet R., 2002, ApJ, 579, 694
Mottram J. C., Hoare M. G., Lumsden S. L., Oudmaijer R. D., Urquhart J. S., Sheret T. L., Clarke A. J., Allsopp J., 2007, A&A, 476, 1019
Mottram J. C., Hoare M. G., Lumsden S. L., Oudmaijer R. D., Urquhart J. S., Meade M. R., Moore T. J. T., Stead J. J., 2010, A&A, 510, A89
Mottram J. C. et al., 2011a, ApJ, 730, L33
Mottram J. C. et al., 2011b, A&A, 525, A149
Norberg P., Maeder A., 2000, A&A, 359, 1025
Patel N. A. et al., 2005, Nat, 437, 109
Petrov R. G. et al., 2007, A&A, 464, 1
Qiu K., Zhang Q., Beuther H., Fallscheer C., 2012, ApJ, 756, 170
Robitaille T. P., Whitney B. A., Indebetouw R., Wood K., 2007, ApJS, 169, 328
Rothman L. S., Rinsland C. P., Goldman A., Massie S. T., Edwards D. P., Flaud J.-M., Perrin A., 1998, J. Quant. Spec. Radiat. Transf., 60, 665
Shakura N. I., Sunyaev R. A., 1973, A&A, 24, 337
Shu F. H., Adams F. C., Lizano S., 1987, ARA&A, 25, 23

Sridharan T. K., Beuther H., Schilke P., Menten K. M., Wyrowski F., 2002, ApJ, 566, 931
Tatulli E. et al., 2008, A&A, 489, 1151
Urquhart J. S., Busfield A. L., Hoare M. G., Lumsden S. L., Clarke A. J., Moore T. J. T., Mottram J. C., Oudmaijer R. D., 2007a, A&A, 461, 11
Urquhart J. S. et al., 2007b, A&A, 474, 891
Urquhart J. S. et al., 2008, A&A, 487, 253
Urquhart J. S. et al., 2009a, A&A, 507, 795
Urquhart J. S., Morgan L. K., Thompson M. A., 2009b, A&A, 497, 789
Urquhart J. S. et al., 2011, MNRAS, 410, 1237
Urquhart J. S. et al., 2012, MNRAS, 420, 1656
Vaidya B., Fendt C., Beuther H., 2009, ApJ, 702, 567
van Dishoeck E. F., Black J. H., 1988, ApJ, 334, 771
Walsh A. J., Hyland A. R., Robinson G., Burton M. G., 1997, MNRAS, 291, 261
Wheelwright H. E., Oudmaijer R. D., de Wit W. J., Hoare M. G., Lumsden S. L., Urquhart J. S., 2010, MNRAS, 408, 1840
Wheelwright H. E., de Wit W. J., Oudmaijer R. D., Hoare M. G., Lumsden S. L., Fujiyoshi T., Close J. L., 2012a, A&A, 540, A89
Wheelwright H. E., de Wit W. J., Weigelt G., Oudmaijer R. D., Ilee J. D., 2012b, A&A, 543, A77
Wolfire M. G., Cassinelli J. P., 1987, ApJ, 319, 850
Wyrowski F., Güsten R., Menten K. M., Wiesemeyer H., Klein B., 2012, A&A, 542, L15
Zinnecker H., Yorke H. W., 2007, ARA&A, 45, 481

APPENDIX A: NOTES ON INDIVIDUAL OBJECTS AND COMPARISON OF RESULTS WITH PREVIOUS STUDIES

Here we discuss and compare, on an object-by-object basis, our findings with that of previous studies on a selection of our sample where data were available.

A1 G033.3891+00.1989

The work of Wheelwright et al. (2010) fitted the CO bandhead emission of this object using fixed power-law relations for the disc. They found a disc from 0.24 to 2.0 au, at an inclination of 18°, with an intrinsic linewidth of 20 km s^{-1} (which was not well constrained) and a CO number density of 9×10^{21} cm^{-2}. The inclination, number density and linewidth agree with our best-fitting model within error ranges, but the size of our disc is much larger, due to a shallow temperature gradient.

A2 G287.3716−00.6444

Wheelwright et al. (2010) do not find a satisfactory fit to the CO bandhead of this object assuming a circumstellar disc (with fixed temperature and density profiles), nor an isothermal non-rotating body of CO. They discuss other possible origins for the emission, including a disc with an outer bulge, a dense neutral wind, a shock, or a disc in which the receding side is much brighter than the approaching side. We note that our temperature exponent is close to −0.43, which would be consistent with a flared, irradiated disc (Chiang & Goldreich 1997) which may act in the same way as a disc with an outer bulge.

A3 G308.9176+00.1231 (AFGL 4176)

Wheelwright et al. (2010) find a disc from 1 to 8 au at an inclination of 30°. The size of the disc agrees well with our results, but we find a higher inclination of 67°, with 30° at the lower limit of our error range. Our linewidth of 12.6 km s^{-1} agrees with their value of 14 km s^{-1}; however our inner density is one order of magnitude lower. Boley et al. (2012) find their observations described well by a large circumstellar disc at an inclination of 60°, agreeing with our best-fitting model, and consistent with the prominent blue shoulder in our data.

A4 G310.0135+00.3892

G310.0135+00.3892 (IRAS 13481−6124) has previously been observed in the *K* band by Kraus et al. (2010) who report an elongated structure that is consistent with a disc viewed at a moderate inclination of approximately 45°. Wheelwright et al. (2012a) fitted the SED using a model with an inclination of 32°. Our relatively high inclination of 67° is not well constrained, due to the poor quality of the data, but agrees with these values within the error range.

Kraus et al. (2010) find a temperature gradient of $p \sim -0.4$, which they suggest is consistent with a flared, irradiated disc based on the work of Chiang & Goldreich (1997). We find a temperature gradient of $p = -0.43$, which is consistent with this hypothesis. Our inner disc temperature of 3800 K is warmer than the value of approximately 1500–2000 K assumed in Kraus et al. (2010), but is consistent as we are concerned with a gaseous disc as opposed to a dust disc. We find a smaller inner radius (2.8 au) for our disc than their study (9.5 au).

A5 G332.9868−00.4871

Wheelwright et al. (2012a) determine an inclination of 15° to G332.9868−00.4871, which is far from our reported value of 78° even considering the large error. However, we note that our data have a relatively low signal-to-noise ratio, and no rotational lines in the fourth chip can be observed, thus our fit is likely not the best fit for the object.

A6 G347.0775−00.3927

Wheelwright et al. (2010) find a similar sized disc to our best-fitting model, from 0.5 to 4 au but with a lower inclination of 30°. However, our inclination of 84° is not well defined, and this does lie within our lower error bound. It should also be noted that the bolometric luminosity from the RMS data base used in their study has since been revised to a lower value, which we use here.

A7 IRAS 08576−4334

IRAS 08576−4334 has been extensively studied in recent years. Bik & Thi (2004) model the CO emission using an isothermal disc from 0.2 to 3.6 au, with an inclination angle of 27°, a CO number density of 3.9×10^{21} cm^{-2} and an excitation temperature of 1600 K. Wheelwright et al. (2010) used a similar method, but utilize a disc model with fixed power laws, and show the data to be well fitted with a 0.09–0.78 au disc, at an inclination of 18°, with a CO number density of 7.9×10^{21} cm^{-2} and an intrinsic linewidth of 20 km s^{-1}.

Ellerbroek et al. (2011) find double peaked He I and Fe I emission lines, with a separation of 60–100 km s^{-1}, which they conclude must originate from a circumstellar disc. They suggest IRAS 08576−4334 is likely an intermediate-mass YSO with a mass accretion rate of 10^{-6} to 10^{-5} M$_\odot$ yr^{-1}, obtained from the determination of the outflow mass-loss rate.

In contrast to Bik & Thi (2004) and Wheelwright et al. (2010), we find our observations are best fitted with larger disc from 0.6 to 6.5 au, at an inclination of 65°. We note that data of Wheelwright

et al. (2010) do not have sufficient wavelength range to observe double-peaked emission lines beyond 2.297 μm, and that the lower resolution of the Bik & Thi (2004) data may mask the presence of these features, especially as they are not well defined and asymmetric in our data. Our best-fitting model possesses a double peak width of approximately 50 km s^{-1}, similar to that of the He I and metal emission lines in Ellerbroek et al. (2011).

We note that the rotationally broadened lines from 2.306 to 2.309 μm show asymmetry, with a depletion on the blue side. These transitions likely correspond to the cooler material further out in the disc, and as such may be evidence for asymmetry in the disc, which cannot be fitted with our axisymmetric disc model.

A8 IRAS 16164−5046

Bik & Thi (2004) model the CO emission of IRAS 16164−5046 using an isothermal disc from 3.1 to 3.2 au (with large errors) at an inclination of 30°, with an excitation temperature of 4480 K and a number density of 4×10^{20} cm^{-2}. The extent of the disc is consistent with our results within errors; however we find a best fit that is closer to the central star, which would account for our larger inner number density. Our disc inclination of 53° is higher.

Bik et al. (2006) find CO emission and Pfund series emission with a width comparable to that of the CO emission, suggesting a common kinematic origin. However, due to the different conditions required for both emission, they suggest the CO emission comes from the midplane of a disc, while the Pf-lines comes from the ionized upper layers. They also note CO absorption from 2.33 to 2.35 μm, indicative of cold, foreground molecular gas.

A9 M8E-IR

Wheelwright et al. (2010) were able to fit the emission of this object with a disc from 0.3 to 2.6 au at an inclination of 16°, with an inner number density of 1×10^{23} cm^{-2} and a linewidth of 7 km s^{-1}. Linz et al. (2009) find an inclination of 18°.5 and a density exponent of $q = -2.05$ using $\alpha = 0.013$.

Our fits to M8E-IR did not satisfactorily converge using many starting positions across the initial parameter space. The spectrum was highly reddened, and the fit suffered from several minima with similar χ^2_r values. The only change applied between these fits was the level of continuum subtraction applied. There were two issues with the data. First, the level of chip four flux seemed too high to be reproduced by the model, meaning that even solutions that reproduced the rotational line structure were assigned poor χ^2_r values. Secondly, the model was unable to reproduce the relatively narrow structures on the red side of the bandhead edge, which may be noise. Because these features were across a larger range of wavelength than the three broader lines at the edge of chip three, the fitting routine assigned them a higher weight which resulted in poor fits to the bandhead slope and the broader lines.

To address this, we restricted the range of fitting to exclude this region (as can be seen in Fig. 4), and increased the allowed upper linewidth to 60 km s^{-1}, which produced a better fit to the data, and produced similar best-fitting parameters similar to those in Linz et al. (2009).

APPENDIX B: NON-MYSO SOURCES AND OBJECTS THAT WERE NOT FITTED

The objects G332.9457+02.3855 and G338.5459+02.1175 were originally thought to be MYSOs at the time of observing, but

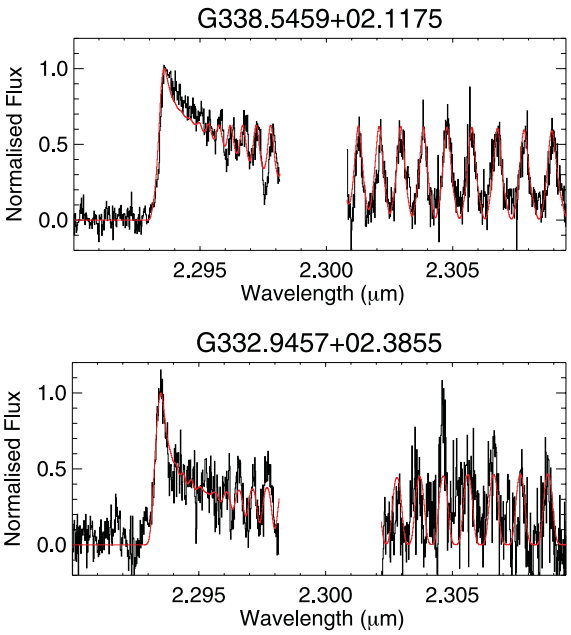

Figure B1. Objects that were later confirmed to be non-MYSO sources, but possess strong CO emission and were fitted with our disc model.

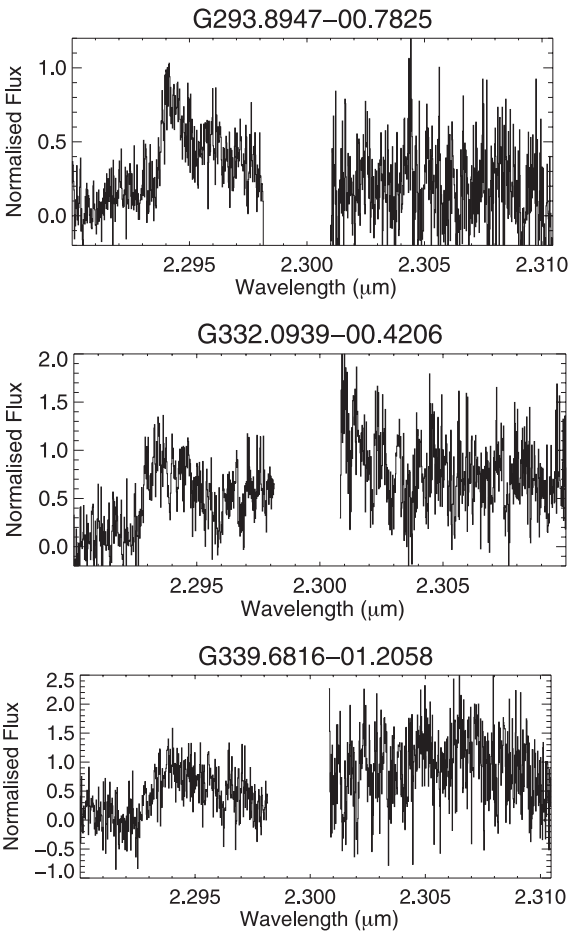

Figure B2. Objects that possessed CO emission that was too weak for an accurate fit to be obtained.

subsequent determination of their bolometric luminosity has shown the objects too faint for this to be the case, and they are likely lower mass young stellar objects. We could not base our estimation of their stellar parameters on the main sequence relationships, so we have estimated their stellar parameters at the values shown in Table 4, which lie in the range of typical T Tauri star values. Changes to these parameters within these ranges had little effect on the final fits. The fits are presented in Fig. B1.

Magnetically channelled accretion funnels have been suggested as a possible source for CO bandhead emission in T Tauri stars (Martin 1997). We obtain good fits to the data of two young stellar objects using a simple disc model. The sizes of the discs are beyond the typical co-rotation radii for these objects. In addition, the intrinsic linewidths of both objects are similar to those of the massive YSOs. This suggests that the emission originates from circumstellar discs regardless of the mass of the central YSO, and not from accretion funnels.

Finally, we note that three objects in the sample had CO emission that was too weak, or a signal-to-noise ratio that was too low for an accurate fit to be obtained. For completeness, we include their spectra in Fig. B2.

This paper has been typeset from a TEX/LATEX file prepared by the author.